Magnetically recyclable Co/ZnO@$NiFe_2O_4$ Nano particle catalyst as a highly active and reusable catalyst for hydrazine monohydrate hydrogen generation

Samikannu Prabu and Kung-Yuh Chiang*

Graduate Institute of Environmental Engineering, National Central University, Tao-Yuan city, 32001, Taiwan

Corresponding author: Prof. Kung-Yuh Chiang Email: kychiang@ncu.edu.tw

Contents

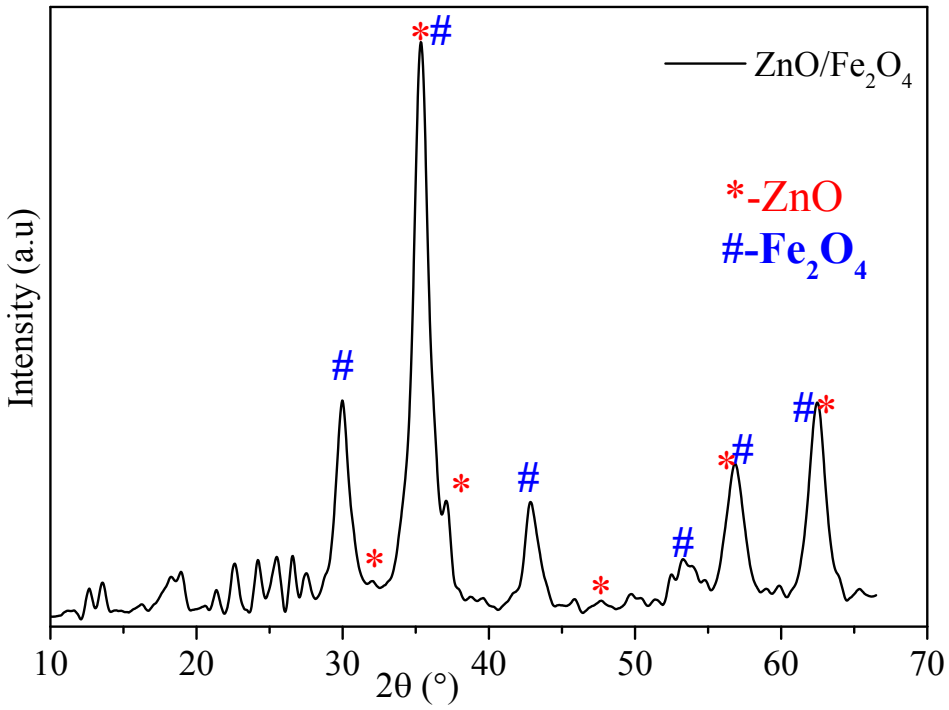

Fig. S1 XRD patterns of ZnO@Fe_2O_4 nanoparticle catalysts.

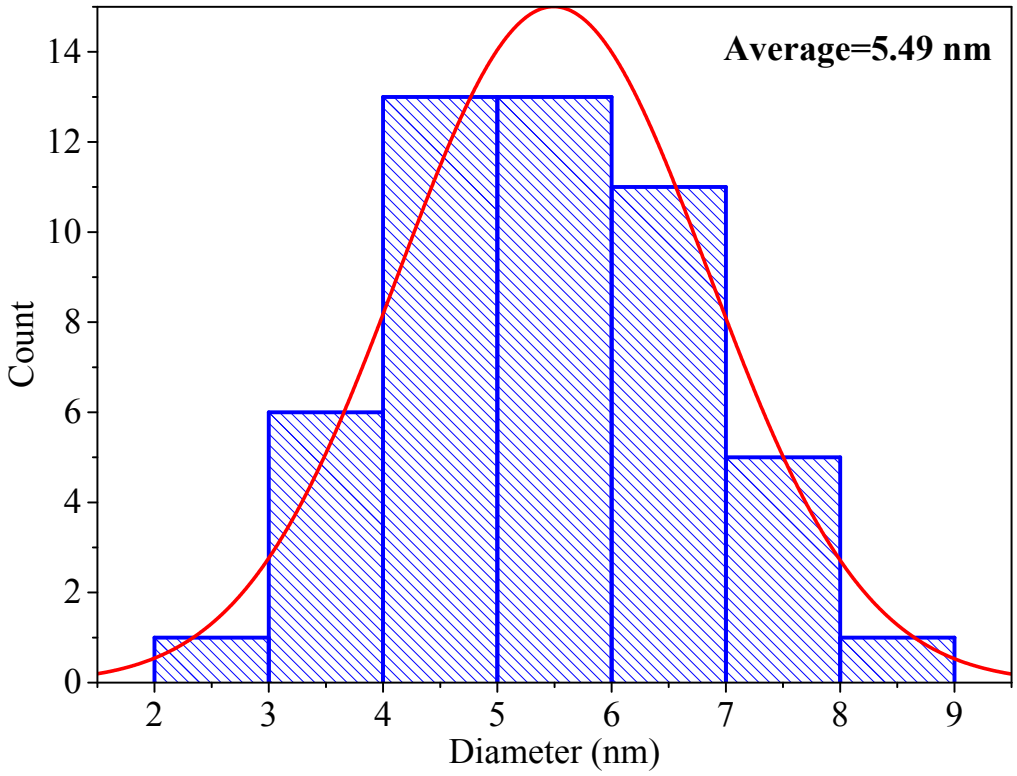

Fig. S2 Co/ZnO@$NiFe_2O_4$ NPs particle size histograms.

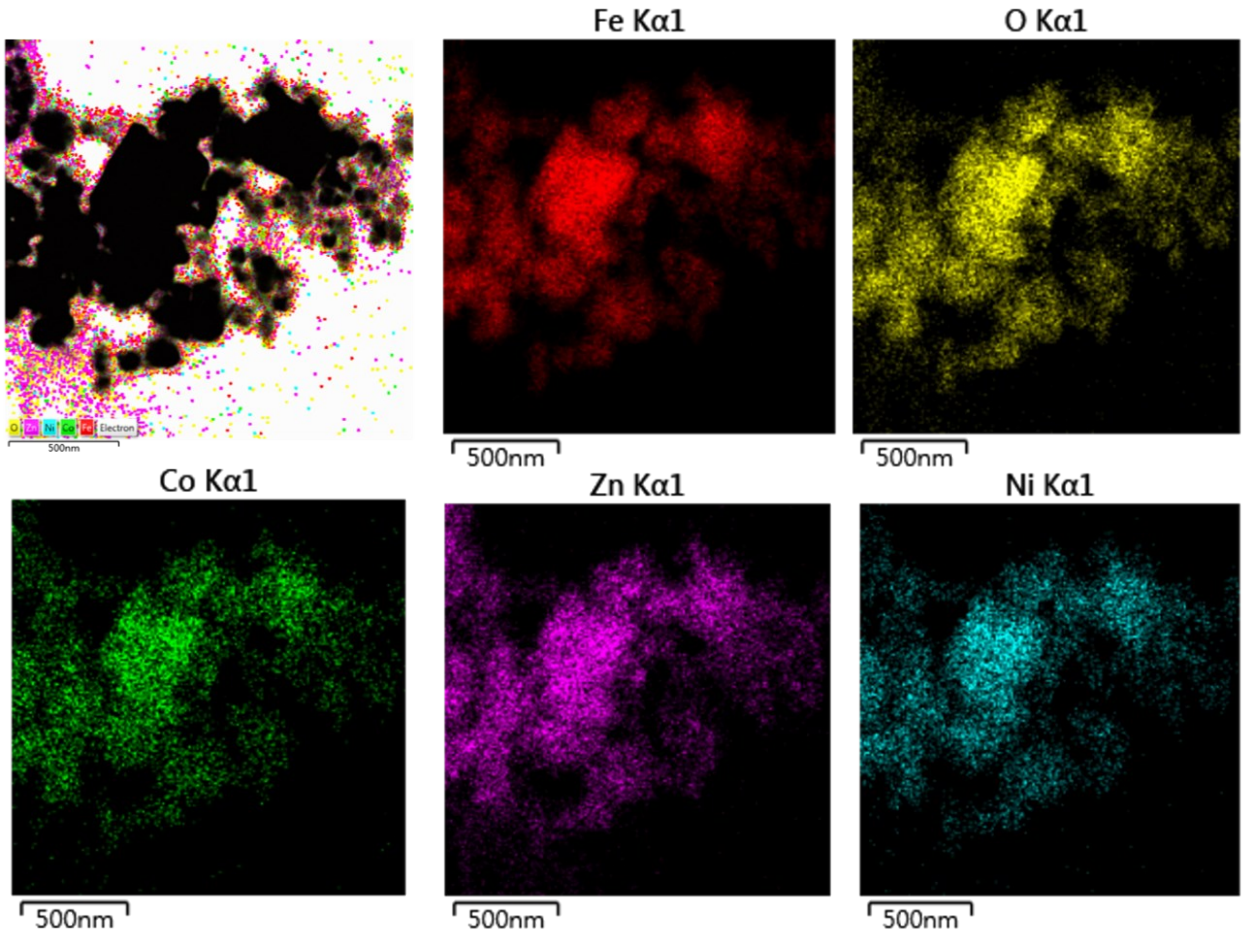

Fig. S3 Co/ZnO@$NiFe_2O_4$ NPs TEM EDX mapping analysis. The scale bar is 500 nm.

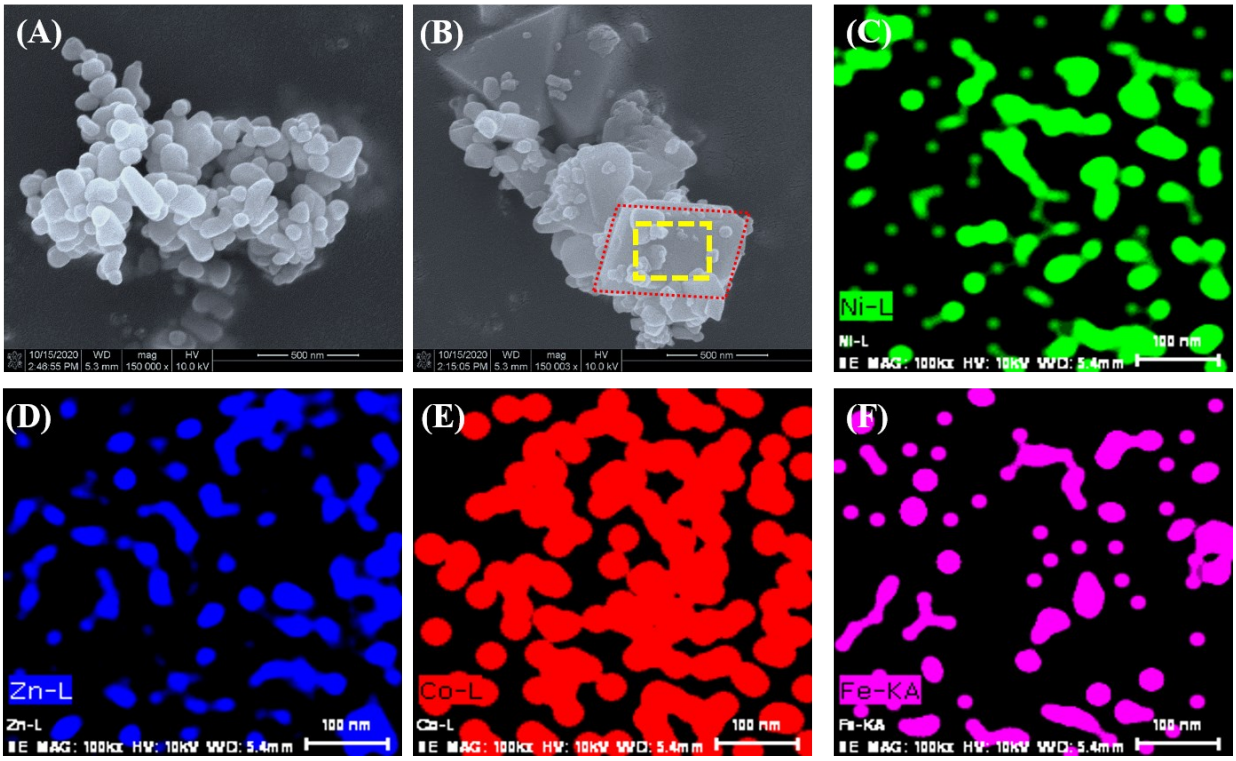

Fig. S4. FE-SEM images of ZnO and Co/ZnO@$NiFe_2O_4$ NPs and elemental mapping analysis of (C) Ni, (D) Zn, (E) Co and (F) Fe, scale bar: 100 nm.

The surface morphology of catalyst is one of the important parameters that affect the hydrogen generation efficiency. The NPs catalysts were investigated by FE-SEM image as shown in **Figure S4** The FE-SEM images shows that the ZnO and Co/ZnO@$NiFe_2O_4$ NPs were formed in a very uniform manner in the form of cubes and a few of them appeared spherically. In order to better discern the composition of the sample, elemental mapping analysis has been done. **Figure S4** (C)~(F) illustrates the Energy-dispersive X-ray spectroscopy (EDX) mapping analysis of Co, Ni, C, Fe, and O for the Co/ZnO@$NiFe_2O_4$ NPs sample. The results confirm the presence of all these elements in the sample which distributed quasi uniformly in the studied section. This result demonstrates the successful preparation of the powder sample.

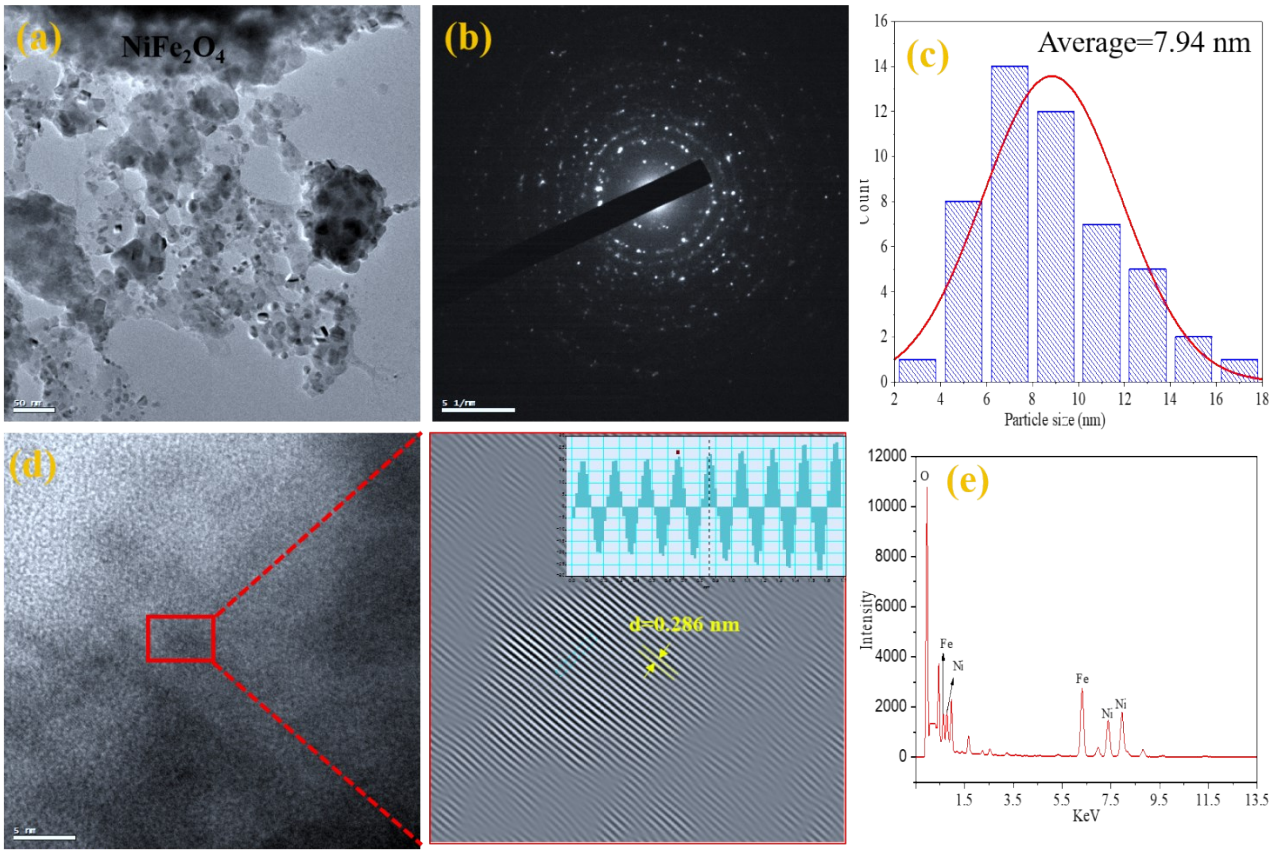

Fig. S5 TEM images of nickel ferrite with the scale bar of (a) 50 nm, and (b) show the corresponding size distribution and SAED patterns, (c) The particle size histograms of $NiFe_2O_4$ NPs , (d) TEM images of nickel ferrite with the scale bar of 5 nm, (e) TEM-EDX spectrum of $NiFe_2O_4$ NPs.

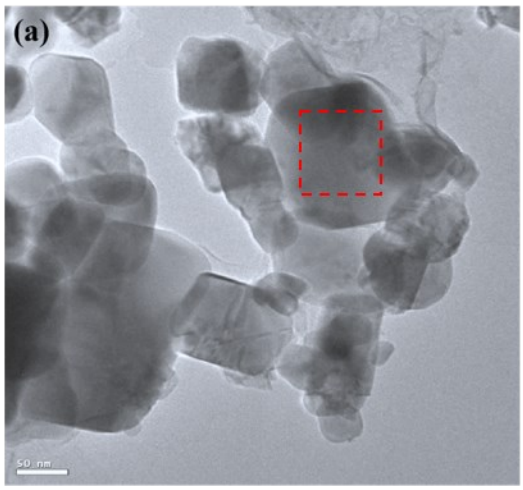

Element	Wt%	Atomic %
O	27.00	56.7
Fe	46.50	29.08
Ni	8.6	4.9
Zn	17.90	9.32
Total:	100.00	100.00

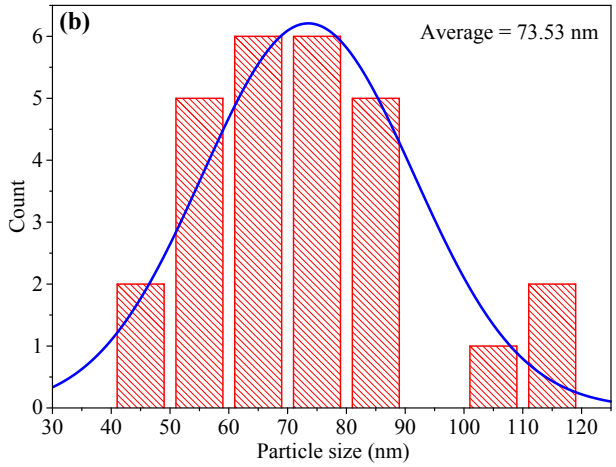

Fig. S6 TEM images of $ZnO@NiFe_2O_4$ NPs (a) and (b) show the corresponding size distribution.

A transition electron microscopy (TEM) image (Fig. S6a) reveals clearly that $NiFe_2O_4$ NPs are coated with ZnO forming a core and shell structure, with an average particle size of 73.53 nm (Fig. S6b). This structure facilitates electron transfer in composite (between $NiFe_2O_4$ and ZnO) and gives the benefit to hydrogen generation from **decomposition of hydrazine in aqueous solution**. Further $ZnO@NiFe_2O_4$ NPs TEM EDX spectrum with a cobalt load of 2.0 wt%, indicating that cobalt is the only element detected in the sample in addition to the $ZnO@NiFe_2O_4$ NPs (O, Ni, Fe, Zn) framework elements.

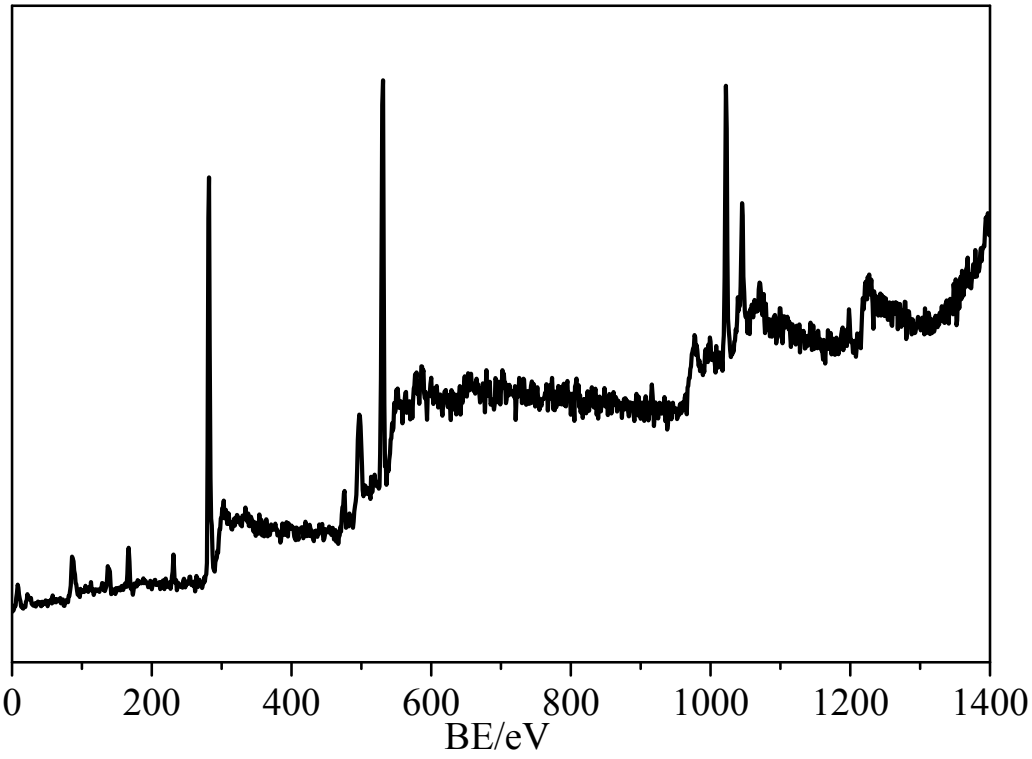

Fig. S7 the XPS spectrum of the fresh Co/ZnO@$NiFe_2O_4$ NPs.

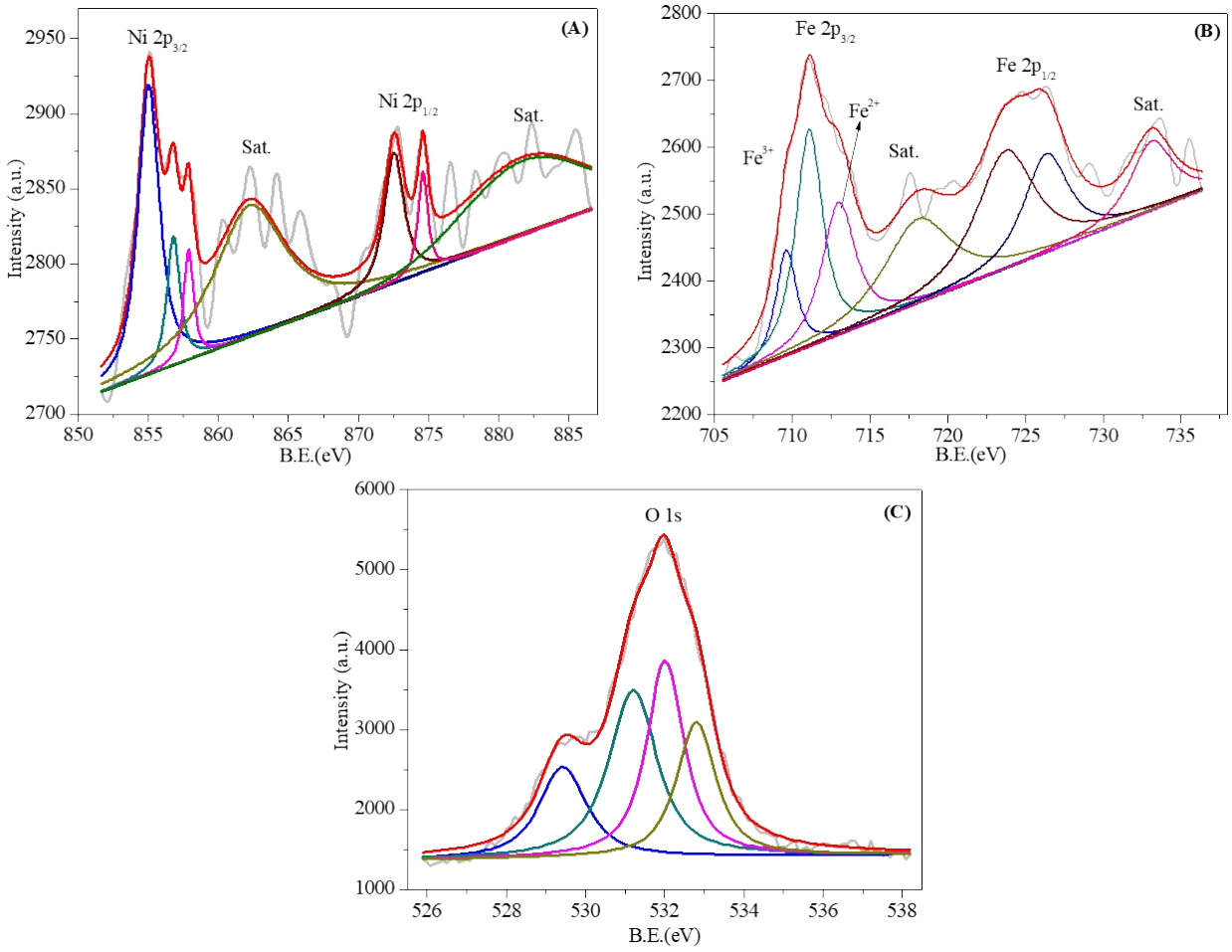

Fig. S8 XPS spectra of (a) Ni 2p, (b) Fe 2p, (c) O 1s for $NiFe_2O_4$ NPs.

Fig. S8 describes the Ni 2p (Fig. S7a), Fe 2p (Fig. S8b), and O 1s (Fig. S8c) core-level XPS spectra for $NiFe_2O_4$ calcined at 750 °C, respectively. The peaks with BE of 855.30 eV refer to the Ni^{2+} ions in the lattice.[S1] Meanwhile, there is a BE component at 855.10 eV consistent to reduced Ni^{2+}, which is well-known to occur as a result of the high $NiFe_2O_4$ NPs catalyst crystallization at this temperature. Ni deficiency sites occur on the surface, or corresponding to the high $NiFe_2O_4$ NPs catalyst crystallization, in which the Ni atoms migrate Ni^{3+} (857.01 eV) to the most favorite crystalline sites.

The XPS spectrum of Fe 2p core-level calcined at 750 °C is depicted in Fig. S8b. Three components were identified: at BE of 710.99 eV (Fe $2p_{3/2}$) and 724.90 eV (Fe $2p_{1/2}$) corresponding to Fe^{3+} ions present in the tetrahedral and the octahedral sites of the spinel structure, respectively. The high binding energy (HBE) component with BE of 717.54 eV might be the satellite shake-up structure of tetrahedral and octahedral ions. After calcination at 850 °C (Fig. S8b), no significant changes were observed in the Fe 2p core-level of $NiFe_2O_4$ NPs. Fig. S8c shows the O 1s spectra. The peak at 529.55 eV is assigned to the contribution of crystal lattice oxygen. Additionally, the peaks at 531.90 are ascribed to the defects, impurities, and captivated oxygen on the spinal surface.[S2]

It has been reported that hydrazine decomposition ($N_2H_4 \rightarrow N_2(g) + 2H_2(g)$) may proceed through different pathways related to the reaction conditions including reaction temperature. In one pathway, N_2 is formed intra-molecularly and not by the recombination of nitrogen species (equation I-1 to I-5).

Pathway-I

$$H_2NNH_2 \rightarrow N_2H_3^* + H^* \text{ …… (I-1)}$$

$$N_2H_3^* \rightarrow N_2H_2^* + H^* \text{ …… (I-2)}$$

$$H^* + H^* \rightarrow H_2(g) \text{ …….. (I-3)}$$

$$N_2H_2^* \rightarrow N_2H^* + H^* \text{ …… (I-4)}$$

$$N_2H^* \rightarrow N_2(g) + H^* \text{ ……..... (I-5)}$$

$$H^* + H^* \rightarrow H_2(g) \text{ …… (I-6)}$$

In the second pathway the N-N bond breaks to form the NH_2 species on the surface [Equation (II-1)], which further decomposes into nitrogen and hydrogen [Equation (II-3) and (II-4)]. It has been

reported that activity energy (Ea) for one pathway is always smaller than Ea for the second pathway.

Pathway-II

$$H_2NNH_2 \rightarrow NH_2^* + 2H^* + N^* \ldots\ldots \text{(II-1)}$$

$$NH_2^* \rightarrow N^* + 2H^* \ldots\ldots\ldots\ldots\ldots \text{(II-2)}$$

$$N^* + N^* \rightarrow N_2\,(g) \ldots\ldots\ldots\ldots\ldots\ldots \text{(II-3)}$$

$$2H^* + 2H^* \rightarrow 2H_2\,(g) \ldots\ldots\ldots\ldots \text{(II-4)}$$

At lower temperatures, the Ea value is 44.84 kJ/mol, indicating that the second hydrazine decomposition pathway is increasing. This is the reason the H_2 evolution plots at higher temperatures slightly faster than those at lower temperatures.

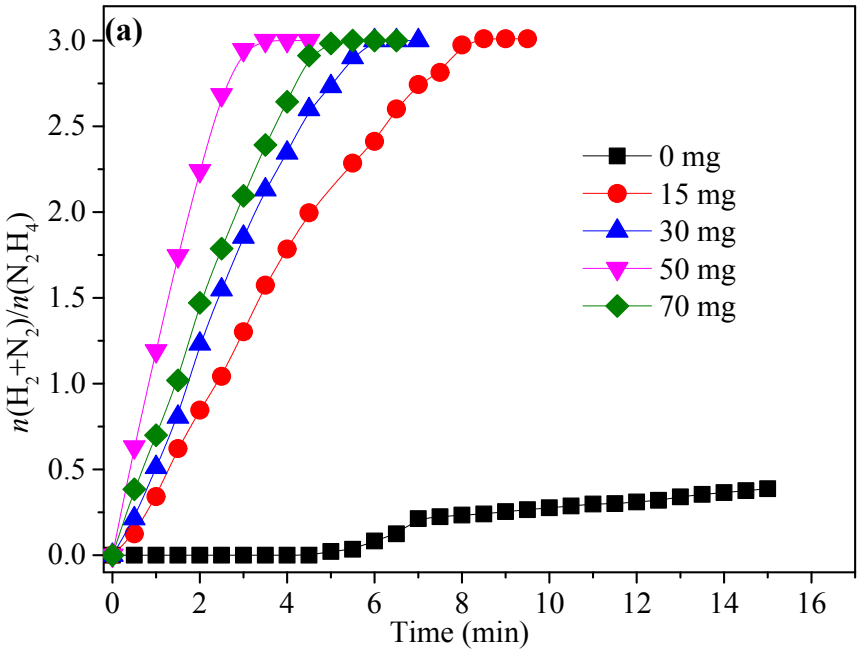

1

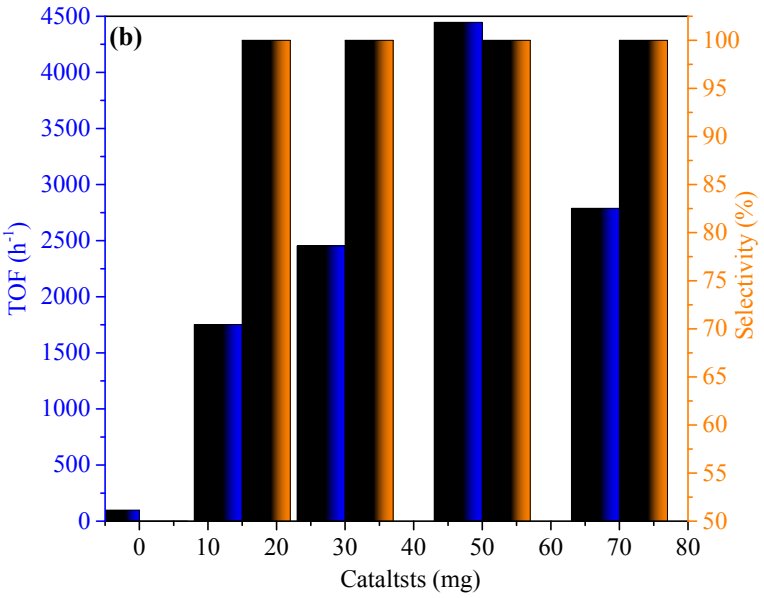

2

3 **Fig. S9** (a) Time course plots and (b) the corresponding TOF values and hydrogen selectivity for

4 hydrogen generation from aqueous N_2H_4 solution (2 mmole, T =25 °C) and different amount of

5 Co/ZnO@$NiFe_2O_4$ NPs catalysts with 2.0 M NaOH (Co+Ni+Fe/N_2H_4 = 0.02).

6

7

Fig. S10 demonstrates the XPS investigation of used Co/ZnO@$NiFe_2O_4$ NPs, in which the statistics of emitted photoelectrons are given as a function of the binding energy up to 1300 eV. Six photoemission peaks (Co *2p*, Fe *2p*, Ni *2p,* Zn *2p,* O *1s* and C *1s*) perform in the extensive spectra of the Co/ZnO@$NiFe_2O_4$ NPs (Fig. S11). The detailed spectrum of Co *2p* peaks in Fig. S11a are equivalent to Ni *2p* peaks, and the peaks of Co $2p_{3/2}$ and Co$2p_{1/2}$ equally can be fragmented to two peaks with BE values of 778.15, 783.37 eV, and 792.56, 796.60 eV, respectively (Table S1), resemble to Co (III) and Co (II). As a trace of Co (II) in the catalyst surface can be oxidized to Co (III) in the sample load and characterization, Co (III) can be perceived. As seen from Fig. S11b (Fe*2p* spectra), trace iron content resulted in strong peak intensity. Both samples exhibit three peaks at 709.63 eV, 715.98 eV and 723.53 eV, which correspond to the binding energy of Fe^{3+} $2p_{3/2}$, shake-up satellite Fe^{3+} $2p_{3/2}$ and Fe^{3+} $2p_{1/2}$, respectively. The detailed spectrum of Ni *2p* peaks magnified from the wide spectrum of the Co/ZnO@$NiFe_2O_4$ NPs shows two peaks at 856.93 eV and 874.94 eV due to the spin–orbit splitting of $2p_{3/2}$ and $2p_{1/2}$, respectively (Fig. S11c), and two satellite peaks at 861.88 and 883.34 eV are two shakeup type peaks of nickel at the high binding energy side of Ni $2p_{3/2}$ and Ni $2p_{1/2}$. As shown in Fig. S11d, the XPS spectrum of Zn *2p* reveals the binding energies of Zn $2p_{3/2}$ at about 1,021.71 eV and Zn $2p_{1/2}$ positioned at 1,044.95 eV, respectively. The de-convoluted peaks at 528.32 and 530.17 eV correspond to lattice oxygen, oxygen vacancies in the $NiFe_2O_4$ environment and insecurely bound oxygen at the $NiFe_2O_4$ and Zn NP surface, respectively (Fig. S11e). In Fig. S11f, the C 1s spectra of the Co/ZnO@$NiFe_2O_4$ NPs was de-convoluted into three peaks, which corresponds to O–C=O (285.04 eV), C–O (283.62 eV), and C=C (281.79 eV). The results reveal that Co, Fe, Ni, Zn, O and C ions in both samples (before and after **catalytic decomposition of hydrazine in aqueous solution**) have the same valances at the surface and internal.

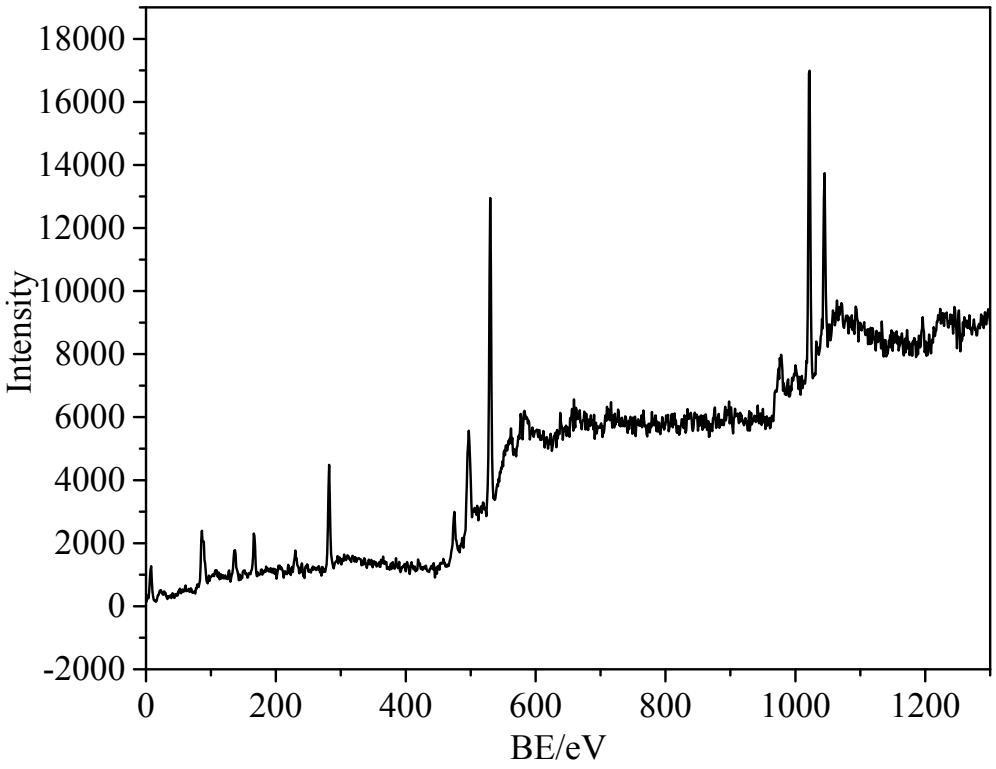

Fig. S10 the XPS spectrum of the used Co/ZnO@$NiFe_2O_4$ NPs.

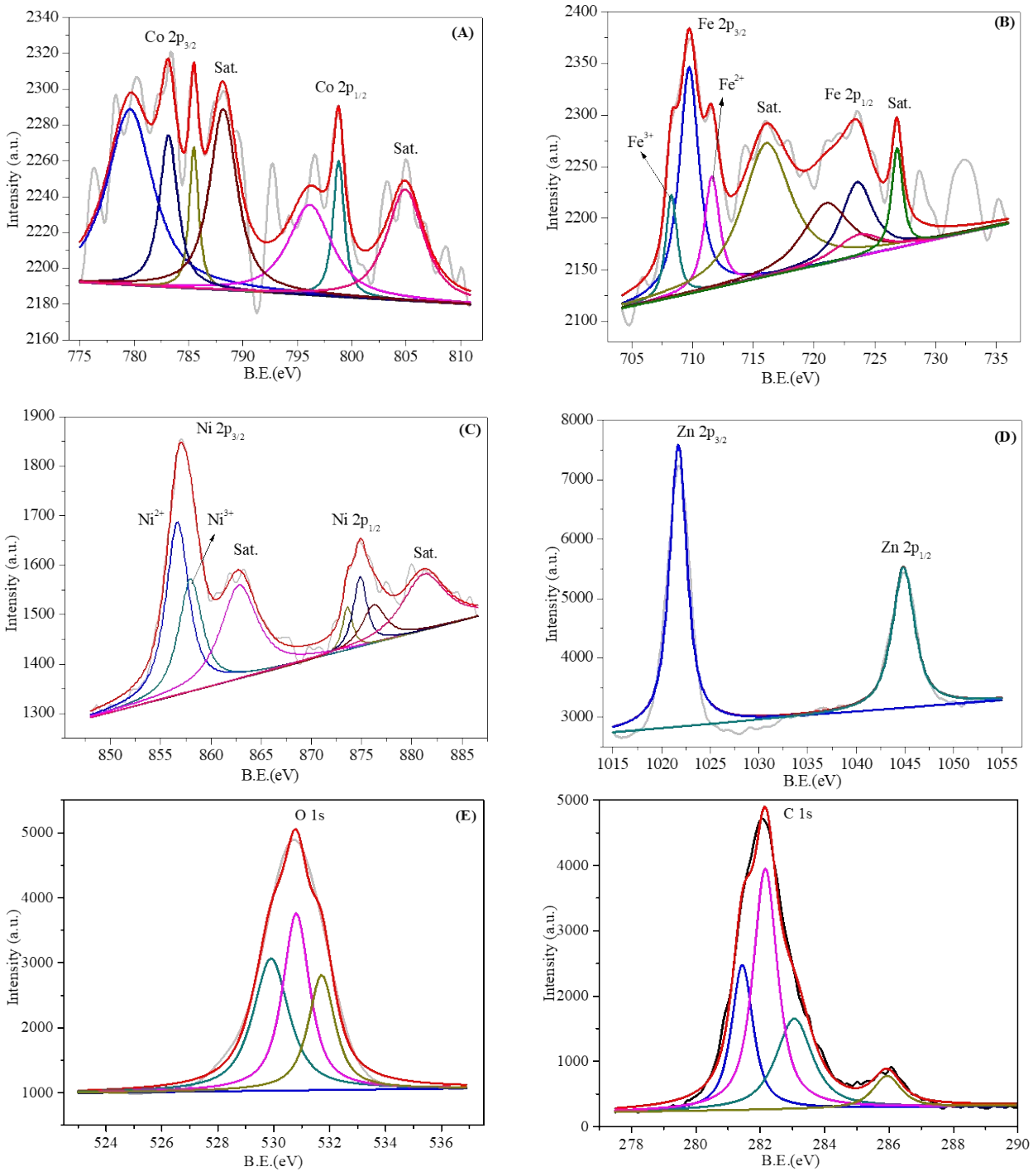

Fig. S11 XPS analysis of Co/ZnO@$NiFe_2O_4$ NPs and detailed analysis of Co *2*p (a), Fe *2*p (b), Ni *2*p (c), Zn *2*p (d), O 1s (e) and C 1s.

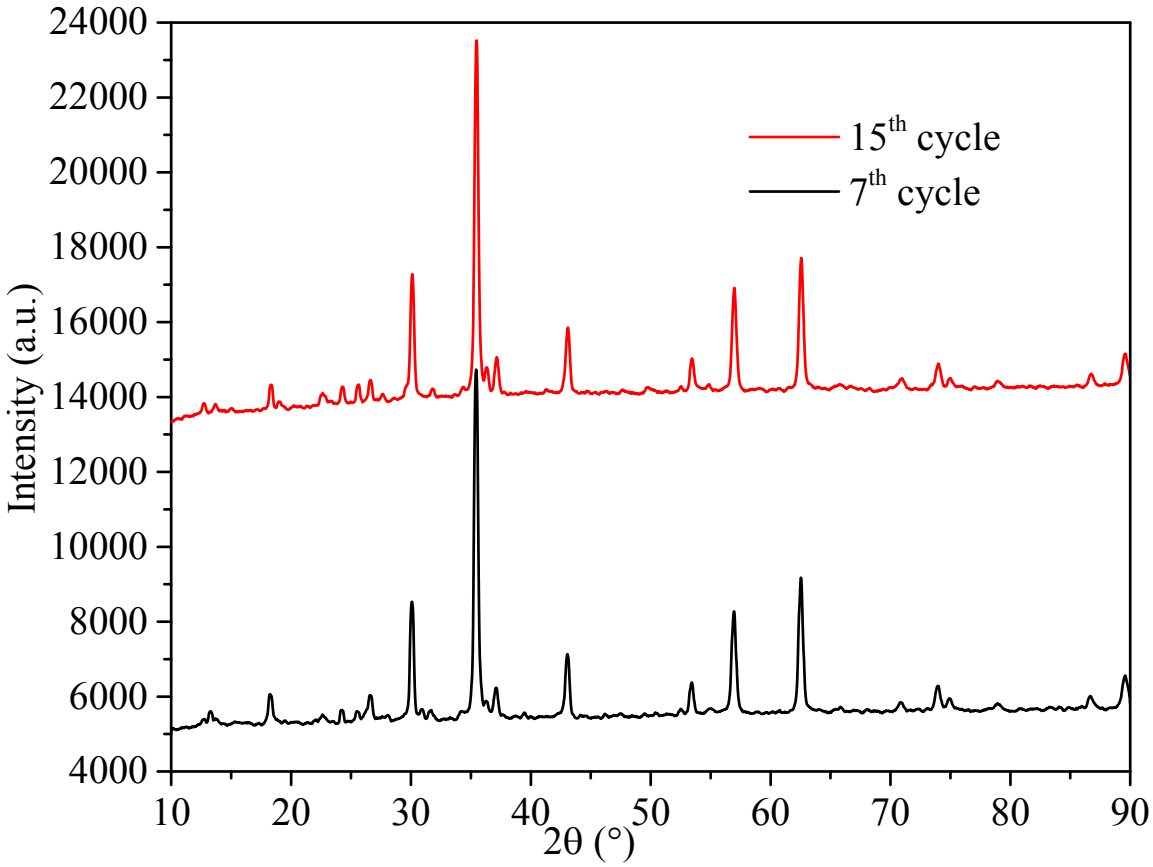

Fig. S12 XRD pattern of the post-used Co/ZnO@$NiFe_2O_4$ NPs catalyst after fifteen cyclic usages.

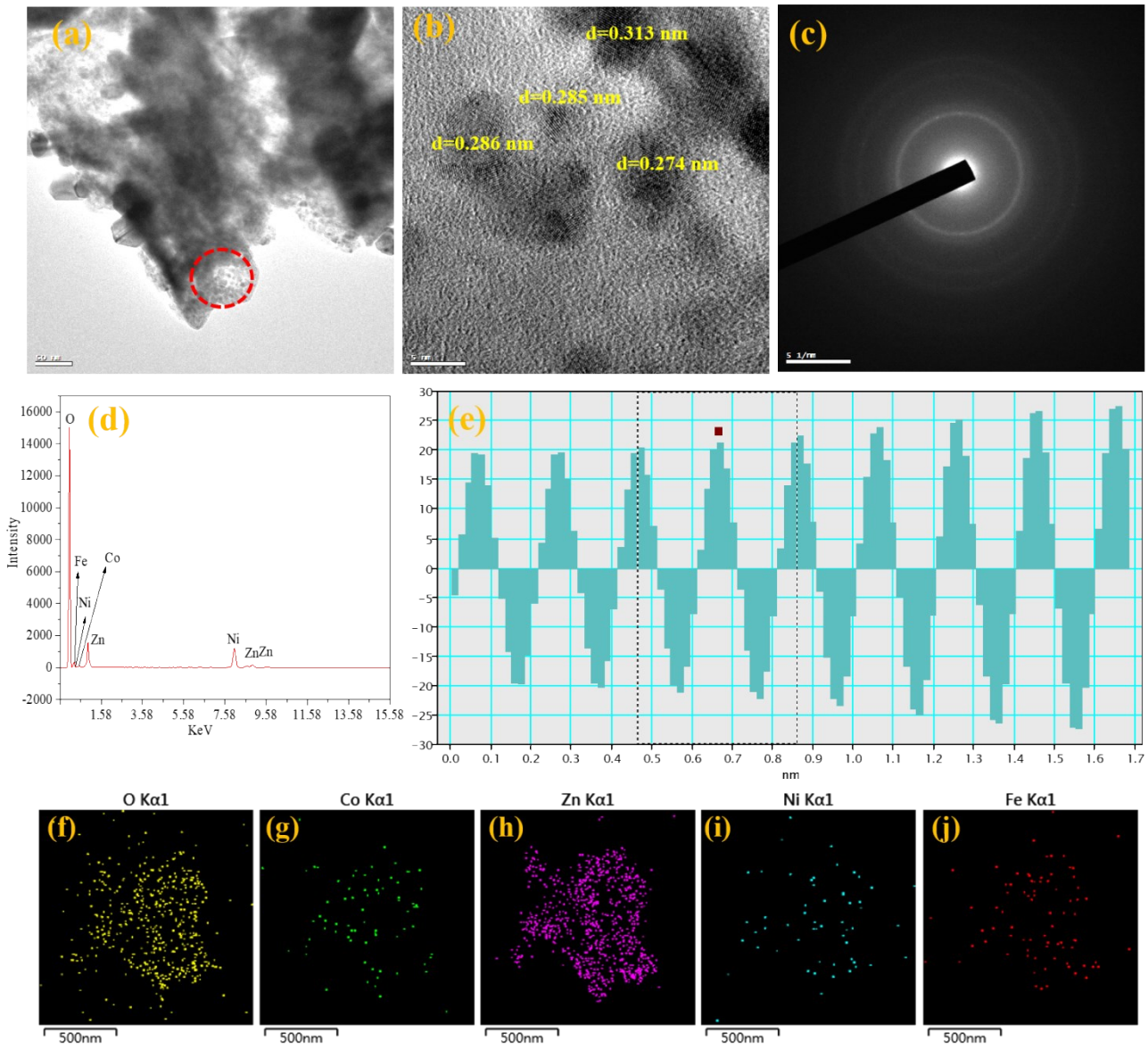

Fig. S13 TEM images of used Co/ZnO@$NiFe_2O_4$ NPs with the scale bar of (a) 50 nm, (b) 5 nm and TEM images of Co/ZnO@$NiFe_2O_4$ NPs with a Co load of 2.0 wt%, (c) show the corresponding size distribution and SAED patterns (d) TEM-EDX spectrum of Co/ZnO@$NiFe_2O_4$ NPs, (e) contrast intensity profile indicates the lattice parameter of Co and (f-j) EDS mapping results.

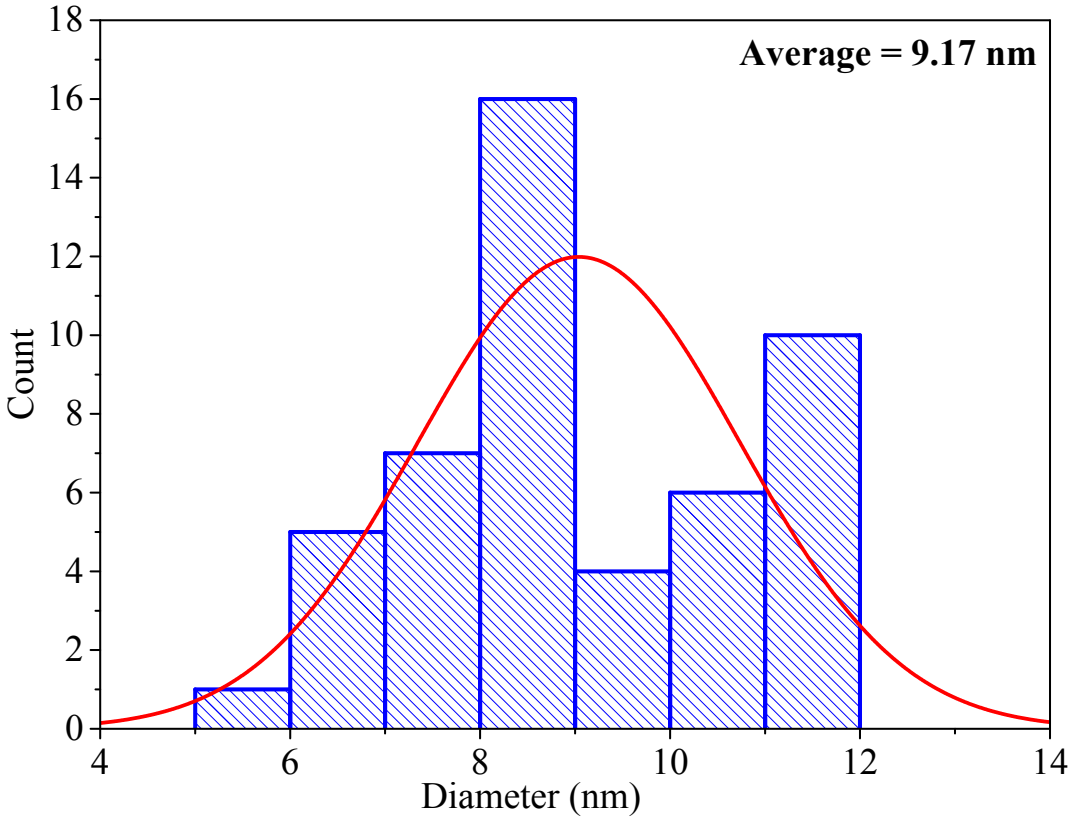

Fig. S14 The particle size histograms of used Co/ZnO@$NiFe_2O_4$ NPs.

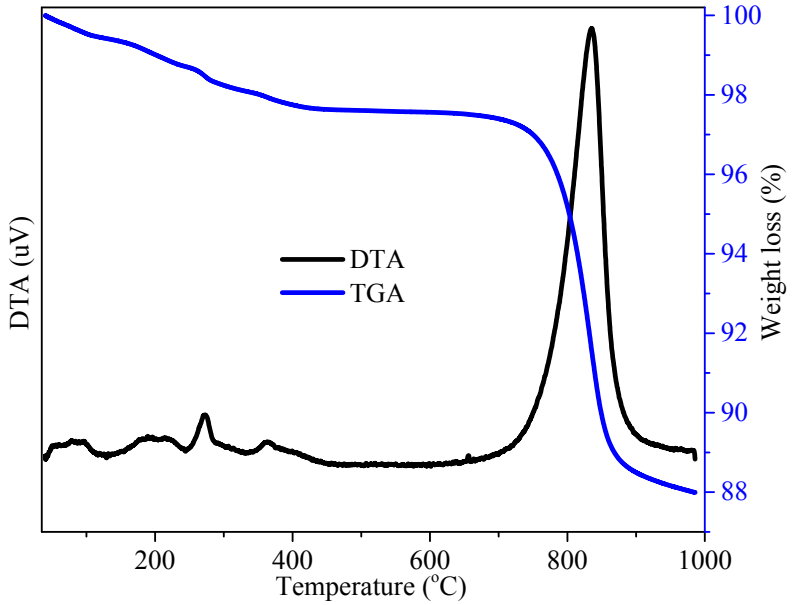

Fig. S15 TGA and DTA curves of Co/ZnO@$NiFe_2O_4$ nanoparticles catalyst.

Table S1. XPS survey data for the elements on the sample surface before and after the decomposition reaction.

Metals	Fresh catalysts				After used catalysts		
	$2p_{3/2}$ eV	$2p_{1/2}$(eV)	Difference	Satellite	$2p_{3/2}$ (eV)	$2p_{1/2}$ (eV)	Satellite (eV)
Co	781.22	797.48	16.21	-	778.15, 783.37	792.56, 796.60	-
Fe	709.79	723..91	14.13	-	709.63, 715.98	723.53	-
Ni	855.07	872.76	17.69	862.25	861.88	883.34	861.88, 883.34
Zn	1022.28	1045.61	23.3	-	1021.71	1044.95	-
O	530.73	529.25	1.48	-	528.32	530.17	-

Table S2. Activities in terms of TOF values of different catalysts tested in hydrogen generation from N_2H_4 aqueous solution.

S.No	Catalysts	Temp. (K)	TOF (h^{-1})	Ea (kJ/mol)	Reusability		Ref.
					Run (No)	Activity (%)	
1.	Pd/Ag/Ni	313	30.2	75.9	5	100	S3
2.	$Ni_{30}Fe_{30}Pd_{40}$	323	21.5	40.0	5	100	S4
3.	$CoRu_{0.11}/\gamma$-Al_2O_3	298	21.9	51.9	3	100	S5
4.	$Pt_{0.2}Ni_{0.8}$/C	323	673	45.7	5	100	S6
5.	NiCo/NiO-CoOx	295	-	45.15	10	99	S7
6.	$Rh_{51}Ni_{19}P_{30}$/rGO	298	101	58.8	5	100	S8
7.	$Rh_{0.7}Ni_{0.3}$/MnOx-MXene	323	1101.9	36.8	6	100	S9
8.	$Rh_{34}Ni_{66}$@ZIF-8	323	140	58.1	5	100	S10
9.	$Ni_{0.9}Pt_{0.1}$/MIL-101	303	140	48.4	8	100	S11
10.	$Rh_{55}Ni_{45}$/$Ce(OH)CO_3$ NCs	323	395	38.8	4	100	S12
11.	$Ni_{0.6}Fe_{0.4}Mo$	323	28.8	50.7	3	100	S13
12.	$Ni_{0.25}Fe_{0.25}Pd_{0.5}$/UiO-66	333	120.3	43.5	5	100	S14
13.	$Ni_{0.6}Pt_{0.4}$/g-C_3N_4 NSs	323	2194	35.9	5	100	S15
14.	NF_{73}	333	6.9	52.07	5	100	S16

15.	$Ni_{0.9}Pt_{0.1}/Ce_2O_3$	298	28.1	42.3	4	100	S17
16.	$Co/ZnO@NiFe_2O_4$	298	4445.37	44.84	15	100	Present work
17.	$Co/ZnO@NiFe_2O_4$	318	11159.14	-	-	100	Present work
18.	$NiIr_{0.059}/Al_2O_3$	303	12.4	38.6	10	99	S18
19.	$Pt_{0.6}Ni_{0.4}@ZrO_2/C/rGO$	323	1920	62.3	5	100	S19
20.	$Ni_{60}Pt_{40}/meso\text{-}CeO_2$	323	1363	58.2	20	100	S20
21.	$Ni_4W/WO_2/NiWO_4$	323	33	-	10	99	S21
22.	$Ni_{10}Mo/Ni\text{-}Mo\text{-}O$	323	54.5	55	10	-	S22
23.	Ni-Mo	303	-	40	10	99	S23
24.	NiPt/NC	323	1602	48.3	10	100	S24
25.	$Ni_{60}Pt_{40}/MNC\text{-}800$	303	1667	32.2	6	100	S25
26.	$Ni_{84}Pt_{16}/graphene$	298	133	40	3	100	S26
27.	$NiPt/La(OH)_3$ $CoPt/La(OH)_3$	323	2400 2400	53.2 45.2	5 5	100 100	S27
28.	$Cu_{0.4}Ni_{0.6}Mo$	323	108		10	100	S28
29.	$Ni_{0.8}Pt_{0.2}/DT\text{-}Ti_3C_2T_x$	323	1220	67.1	-	100	S29

References

1 C. Solis, S. Somacescu, E. Palafox, M. Balaguer and J. M. Serra, *J. Phys. Chem. C*, 2014, **118**, 24266-24273.

2 D. R. Lima, N. Jiang, X. Liu, J. Wang, V. A. Vulcani, A. Martins and A. Pancotti, *ACS Appl. Mater. Interfaces*, 2017, **9**, 39830-39838.

3 K. S. Al-Thubaiti and Z. Khan, *Int. J. Hydrogen Energy*, 2020, **45**, 13960-13974.

4 D. Bhattacharjee and S. Dasgupta, *J. Mater. Chem. A*, 2015, **3**, 24371-24378.

5 N. Firdous, N. K. Janjua and M. H. S. Wattoo, *Int. J. Hydrogen Energy*, 2020, **45**, 21573-21587.

6 J. Wang, A. Khaniya, L. Hu, M. J. Beazley, W. E. Kaden and X. Feng, *J. Mater. Chem. A*, 2018, **6**, 18050-18056.

7 D. Wu, M. Wen, X. Lin, Q. Wu, C. Gu and H. Chen, *J. Mater. Chem. A*, 2016, **4**, 6595-6602.

8 X. Du, S. Tan, P. Cai, W. Luo and G. Cheng, *J. Mater. Chem. A*, 2016, **4**, 14572-14576.

9 B. Yin, Q. Wang, T. Liu and G. Gao, *New J Chem*., 2018, **42**, 20001-20006.

10 B. Xia, N. Cao, H. Dai, J. Su, X. Wu, W. Luo and G. Cheng, *ChemCatChem*., 2014, **6**, 2549-2552.

11 Z. Zhang, S. Zhang, Q. Yao, X. Chen and Z. H. Lu, *Inorg. Chem*., 2017, **56**, 11938-11945.

12 J. Chen, Q. Yao, J. Zhu, X. Chen and Z. H. Lu, *Int. J. Hydrogen Energy*, 2016, **41**, 3946-3954.

13 H. L. Wang, J. M. Yan, S. J. Li, X. W. Zhang and Q. Jiang, *J. Mater. Chem. A*, 2014, **3**, 121-124.

14 X. Song, P. Yang, J. Wang, X. Zhao, Y. Zhou, Y. Li and L. Yang, *Inorg. Chem. Front*., 2019, **6**, 2727-2735.

15 C. Wan, L. Sun, L. Xu, D. G. Cheng, F. Chen, X. Zhan and Y. Yang, *J. Mater. Chem. A*, 2019, **7**, 8798-8804.

16 Q. Fu, P. Yang, J. Wang, H. Wang, L. Yang and X. Zhao, *J. Mater. Chem. A*, 2018, **6**, 11370-11376.

17 H. L. Wang, J. M. Yan, Z. L. Wang, O. Song-Il and Q. Jiang, *J. Mater. Chem. A*, 2013, **1**, 14957-14962.

18 L. He, Y. Huang, X. Y. Liu, L. Li, A. Wang, X. Wang and T. Zhang, *Appl. Catal*., 2014, **147**, 779-788.

19 F. Z. Song, X. Yang and Q. Xu, *Small Methods*, 2020, **4**, 1900707.

20 Y. Y. Jiang, H. B. Dai, Y. J. Zhong, D. M. Chen and P. Wang, *Chem. Eur. J*., 2015, **21**, 15439-15445.

21 Q. Shi, D. X. Zhang, H. Yin, Y. P. Qiu, L. L. Zhou, C. Chen and P. Wang, *ACS Sustain. Chem. Eng*., 2020, **8**, 5595-5603.

22 Y. P. Qiu, G. X. Cao, H. Wen, Q. Shi, H. Dai and P. Wang, *Int. J. Hydrogen Energy*, 2019, **44**, 15110-15117.

23 Y. Wang, L. Pan, Y. Chen, G. Shen, L. Wang, X. Zhang and J. J. Zou, *Int. J. Hydrogen Energy*, 2020, **45**, 15560-15570.

24 Y. P. Qiu, Q. Shi, L. L. Zhou, M. H. Chen, C. Chen, P. P. Tang and P. Wang, *ACS Appl. Mater. Interfaces*, 2020, **12**, 18617-18624.

25 W. Wang, X. Hong, Q. Yao, Z. H. Lu, *J. Mater. Chem. A*, 2020, **8**, 13694-13701.

26 Y. Du, J. Su, W. Luo and G. Cheng, *ACS Appl. Mater. Interfaces*, 2015, **7**, 1031-1034.

27 K. Wang, Q. Yao, S. Qing and Z.H. Lu, J. Mater. Chem A, 2019, **7**, 9903-9911.

28 Q. Yao, Z. H. Lu, R. Zhang, S. Zhang, X. Chen, and H.L. Jiang, J. Mater. Chem A, 2018, **6**, 4386-4393.

29 F. Guo, H. Zou, Q. Yao, B. Huang and Z.H. Lu, *Renew. Energ.,* 2020, **155,** 1293-1301.